Tunability of the Adsorbate Binding on Bimetallic Alloy Nanoparticles for the Optimization of Catalytic Hydrogenation
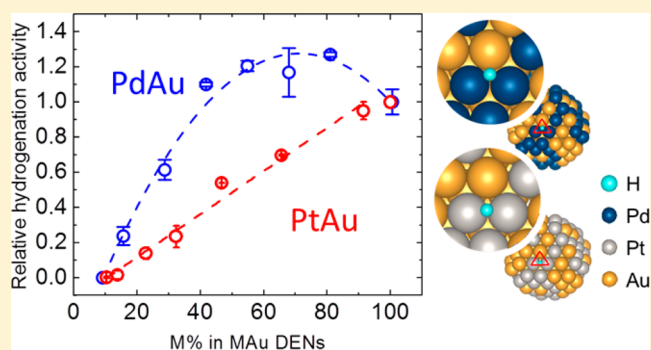
Long Luo,[†,⊥] Zhiyao Duan,[†,‡,⊥] Hao Li,[†,‡] Joohoon Kim,[∥] Graeme Henkelman,*,[†,‡] and Richard M. Crooks*,[†,§]

†Department of Chemistry, ‡Institute for Computational and Engineering Sciences, §Texas Materials Institute, The University of Texas at Austin, 105 E. 24th Street, Stop A5300, Austin, Texas 78712, United States
∥Department of Chemistry, KHU-KIST Department of Converging Science and Technology, Research Institute for Basic Sciences, Kyung Hee University, Seoul, South Korea

Ⓢ Supporting Information

ABSTRACT: In this paper, we show that PtAu and PdAu random alloy dendrimer-encapsulated nanoparticles with an average size of ~1.6 nm have different catalytic activity trends for allyl alcohol hydrogenation. Specifically, PtAu nanoparticles exhibit a linear increase in activity with increasing Pt content, whereas PdAu dendrimer-encapsulated nanoparticles show a maximum activity at a Pd content of ~60%. Both experimental and theoretical results suggest that this contrasting behavior is caused by differences in the strength of H binding on the PtAu and PdAu alloy surfaces. The results have significant implications for predicting the catalytic performance of bimetallic nanoparticles on the basis of density functional theory calculations.

INTRODUCTION

Catalytic hydrogenation of olefins is important for a wide variety of commercial processes.[1−5] While both mono- and bimetallic catalysts are used for hydrogenations,[6−9] bimetallics are of particular interest because they frequently exhibit superior activity, stability, and selectivity.[6−18] The enhanced performance of bimetallics is usually attributed to either electronic, strain, or ensemble effects. Electronic effects involve the transfer of charge between the two metals, which changes the electronic structure and activity of the constituent atoms.[19] Strain in a metallic surface layer also changes the electronic structure by altering the width and center of the d-band.[20] In contrast, catalytic enhancement due to ensemble effects emphasizes favorable atomic configurations on the nanoparticle surface.[8−10] It has been suggested that ensemble effects play a more significant role than electronic effects when there is heterogeneity in the surface atomic configuration,[8,10] but it is difficult to clearly disentangle the two. As a consequence, the mechanism of enhanced activities of alloy catalysts in olefin hydrogenation is still under debate.

Density functional theory (DFT) calculations are well-suited for developing a better understanding of the relative contributions of electronic and ensemble effects, because they take both into account. For example, DFT calculations have been used to investigate the hydrogenation of simple olefins, such as ethylene, on metallic surfaces, including Pt, Pd, and Ru.[21−24] These results showed that hydrogenation proceeds primarily via the Horiuti−Polanyi (H−P) mechanism. In the

H−P mechanism, both the olefin and H_2 are first adsorbed onto the catalyst surface. H_2 then dissociates into a pair of adsorbed H atoms (H_{ads}). The reaction then proceeds via two sequential hydrogen additions to yield the saturated hydrocarbon product. The reaction rate is determined by the activation energies of the two hydrogen addition steps.[21,23] Recently, Henkelman and co-workers reported that these activation energies were correlated with the binding energies of H_{ads} and the olefin on the catalytic surface.[25,26]

As an example of how binding energies can be used to predict reaction rates, Figure 1 shows a calculated activity plot for hydrogenation of allyl alcohol (AA) as a function of H_{ads} and AA_{ads} binding energies ($E_{H,b}$ and $E_{AA,b}$). Details regarding the origin of this plot are provided in the Supporting Information (SI; including Figures S1 and S2 and Tables S1 and S2). The results show that most monometallic surfaces (green circles) and their corresponding 140 atom clusters (blue squares) are not predicted to display the theoretical maximum activity (indicated by the white square at the center of the plot), because they bind the two reactants (H_{ads} and AA_{ads}) either too strongly or too weakly. In contrast, bimetallic surfaces may exhibit enhanced activity because of the presence of new atomic surface configurations that move these binding energies closer to the optimal value. The difficulty lies in how to properly choose two metals that lead to optimal binding energies. One
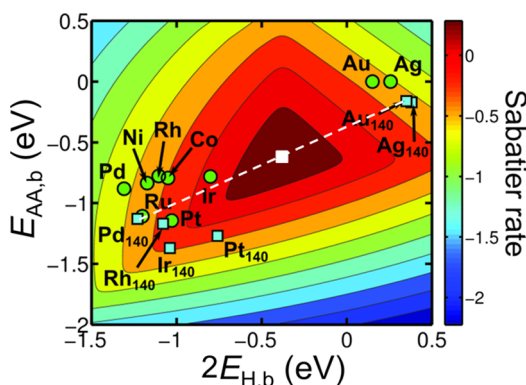
Figure 1. Contour plot of the Sabatier rate as a function of the H and AA adsorption energies ($E_{H,b}$ and $E_{AA,b}$, respectively) on bulk metals (green circles) and 140 atom clusters (blue squares). The procedure used for constructing this plot is provided in the Supporting Information.

strategy is to select two metals on opposite sides of the activity volcano (Figure 1). This approach is based on the hypothesis that mixing strong- and weak-binding metals generates medium-binding bimetallics (white dashed line in Figure 1), which are located closer to the volcano center (white square in Figure 1). Prior studies carried out by us and others have confirmed the viability of this method for alloys that include RhAu, RhAg, and PdAu.[25−27]

In this paper, we closely examine this volcano-plot-based design strategy and explore its applicability and limitations using both experiments and DFT calculations. Specifically, we synthesized and characterized well-defined, sub-2 nm PtAu and PdAu random alloy dendrimer-encapsulated nanoparticles (DENs)[28,29] and then evaluated their activities for AA hydrogenation.[30,31] The experimental results show that PtAu DENs exhibit monotonically increasing activity with increasing Pt content, while PdAu DENs achieve maximum activity at a Pd content of ~60%. These observations show that the optimization strategy represented by the white dashed line in Figure 1 applies to PdAu DENs but not to PtAu DENs, even though Pt and Pd are similar in terms of $E_{H,b}$ and $E_{AA,b}$ relative to Au (Figure 1).

DFT calculations suggest that the differences in composition-dependent activity arise from different tunabilities of $E_{H,b}$ on the two alloy surfaces. Specifically, the presence of Au in the PtAu alloy DENs does not significantly affect $E_{H,b}$, and therefore Au simply acts as a diluent to reduce the overall number of Pt surface sites, thereby reducing activity. In contrast, PdAu alloy DENs can exhibit higher activities than their individual metal constituents, because their $E_{H,b}$ can be tuned to the most desirable value using the approach highlighted in Figure 1. DFT also suggests that the tunability of $E_{H,b}$ is associated with optimal H binding geometries at specific bimetallic surface−atom ensembles. This finding is significant, because it provides new guidance for the rational design of bimetallic catalysts for catalytic hydrogenations and perhaps other reactions as well.

■ RESULTS AND DISCUSSION

Catalyst Synthesis and Characterization. The MAu (M = Pt or Pd) DENs used in this study were synthesized by co-complexation of either K_2PtCl_4 or K_2PdCl_4 and $HAuCl_4$ with G6OH dendrimers, followed by $NaBH_4$ reduction.[32] The

formula $M_xAu_{1−x}$ is used to represent the specific composition of the resulting DENs, where x is the molar percentage of M in the corresponding nanoparticles. For $Pd_xAu_{1−x}$ DENs, x was calculated by correlating the molar percentages of $PdCl_4^{2−}$ and $AuCl_4^{−}$ used in the DEN precursor to produce the final DENs. As we have shown previously, this is a reliable method because both precursor ions are completely reduced to Pd^0 and Au^0 by $NaBH_4$.[33] For $Pt_xAu_{1−x}$ DENs, however, x was determined by XPS, because less than 100% of intradendrimer $PtCl_4^{2−}$ is reduced to Pt^0. Additional discussion of this point is provided in the SI (Figures S3−S5).[34] Note also that Pd and $Pd_xAu_{1−x}$ DENs were always prepared within 1 h of use and kept under N_2, because Pd slowly oxidizes in air.[33] The other DENs were stable in air, so they were synthesized in advance, dialyzed, and then stored at 7 °C prior to use.

$M_xAu_{1−x}$ DENs prepared by the co-complexation route were characterized by transmission electron microscopy (TEM, Figure S6). The analysis of at least 100 randomly selected $M_xAu_{1−x}$ DENs indicates an average size of ~1.6 ± 0.4 nm, regardless of composition. This is identical to the calculated diameter (1.6 nm) of a 140-atom $M_xAu_{1−x}$ nanoparticle having a truncated octahedral shape.[32,35]

In addition to their size, it is also necessary to have accurate information about the structure of these bimetallic NPs. This is particularly important here, because Pd and Au are completely miscible, at least in bulk alloy form, but Pt and Au are not.[36,37] Energy-dispersive X-ray spectroscopy (EDX) is often used for elemental mapping,[38,39] but the small size (<2 nm) of bimetallic DENs renders this approach insufficiently accurate.[40] An alternative method for determining the structure of bimetallic DENs is extended X-ray absorption fine structure (EXAFS) spectroscopy, which probes the local atomic environment around one specific element.[33,40−42] Our group has previously examined $Pd_xAu_{1−x}$ DENs using EXAFS and found them to be quasirandom alloys with a slightly Au-rich core and a slightly Pd-rich shell.[33] Unfortunately, the same sort of EXAFS analysis of $Pt_xAu_{1−x}$ DENs is less accessible due to the overlapping X-ray absorption edges (L_3 edges) of Pt and Au.[43]

Due to the limitations of TEM and EXAFS, we developed an alternative electrochemical approach for analyzing the surface structure of bimetallic DENs. This method is based on Cu underpotential deposition (UPD) and specifically the fact that the potential required to oxidize a UPD layer of Cu depends on the nature of the underlying metal.[32,44,45] To determine the surface composition of $Pt_xAu_{1−x}$ DENs, for example, a UPD monolayer of Cu was deposited by holding the potential of the DEN-modified electrodes at E_{dep} = −0.38 V (determined by voltammetry) in a solution containing 0.10 M $HClO_4$ and 5.0 mM $CuSO_4$ for 100 s. Immediately after Cu deposition, the potential of the resulting $Pt_xAu_{1−x}$@Cu DENs was scanned from E_{dep} to 0.20 V to oxidize the Cu shell (anodic peaks, Figure 2a). Pt@Cu DENs (x = 1.0) exhibit one broad peak centered at ~ −0.1 V (fwhm = ~300 mV) and one sharper peak at −0.25 V (fwhm ~100 mV), which is consistent with previous findings.[41,42] On the basis of earlier EXAFS studies, these two peaks correspond to the oxidation of Cu on the Pt(100) and Pt(111) facets of the Pt DENs, respectively.[42]

With decreasing Pt content, the two well-defined anodic peaks of the $Pt_xAu_{1−x}$@Cu DENs gradually merge (Figure 2a). These voltammograms were deconvoluted, and the potential of the largest peak plotted as a function of composition (x in $Pt_xAu_{1−x}$) in Figure 2c (red circles). This plot is linear and has a
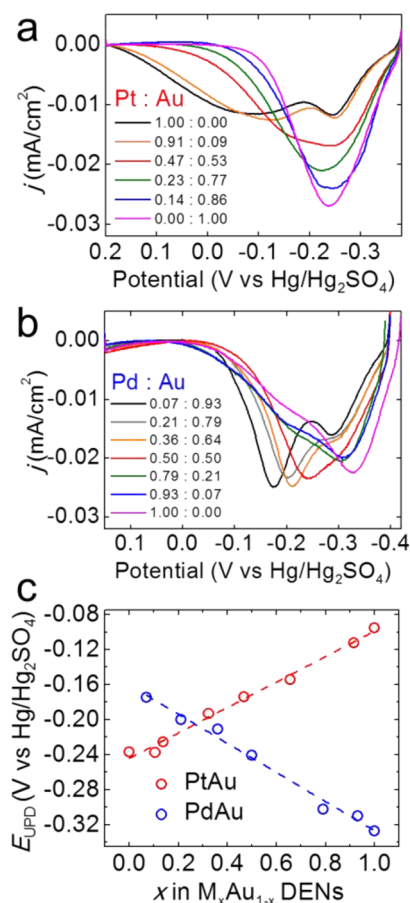
Figure 2. Stripping voltammograms for the oxidation of UPD Cu shells on (a) Pt_xAu_{1-x} and (b) Pd_xAu_{1-x} DENs. The oxidation current is normalized to the electrochemically active surface area of the DENs prior to catalysis, which is calculated from the charge passed during Cu oxidation. The scan rate for all CVs was 10.0 mV/s, and all solutions were degassed with N_2. Peak positions were obtained by fitting two Gaussian distributions to the oxidative waves. (c) Plots of the position of the main peak (E_{UPD}) vs x in M_xAu_{1-x} DENs. The dashed lines are the best linear fits to the data.

slope of 14.5 mV per 10% change in Pt content. This suggests that the surface of Pt_xAu_{1-x} DENs undergoes a smooth compositional transition from Pt to Au, which is consistent with a random alloy model. To further validate this conclusion, we carried out two control experiments.

In the first control experiment, a physical mixture of Pt-only and Au-only DENs (denoted as Pt + Au) was prepared. This mixture represents the extreme case of complete phase segregation of Pt and Au in the Pt_xAu_{1-x} DENs. The voltammograms of the Pt+Au DEN mixtures cross each other at a single point ($\sim$-0.15 V, Figure S7), which is similar to the isosbestic point in spectroscopy. No such point was observed in the voltammetry of Pt_xAu_{1-x} DENs, suggesting no significant phase segregation of Pt and Au in the Pt_xAu_{1-x} DENs.

In the second control experiment, intentionally segregated Au@Pt core@shell DENs (Pt/(Pt + Au) = $\sim$0.4) were used in the same Cu UPD experiment to test whether the surface segregation of Pt takes place in Pt_xAu_{1-x} DENs. The result shows E_{UPD} for Au@Pt DENs is at $\sim$ -0.13 V (Figure S8), 70 mV more positive than Pt_xAu_{1-x} DENs when x = 0.4. This difference is not consistent with the surface segregation of the Pt_xAu_{1-x} DENs. Based on these experimental data, we conclude

that the Pt_xAu_{1-x} DENs are primarily random alloys even though the two elements are largely immiscible in bulk. This conclusion is not entirely surprising because other studies have shown that Pt and Au alloy at the nanoscale.[36,39,46]

Like the Pt_xAu_{1-x} DENs, Pd_xAu_{1-x} DENs also exhibit a linear correlation between E_{UPD} and composition (x in Pd_xAu_{1-x}, Figure 2b and c). The fact that previous EXAFS studies have independently shown these materials to be random alloys[33] provides additional evidence for this correlation to be associated with that structure. Also note that the two lines in Figure 2c do not intersect at x = 0, which would be expected because in this case both DENs are composed of only Au. The reason the lines do not intersect at x = 0 is subtle: the Pd_xAu_{1-x} DENs were used without dialysis (due to their instability in air), whereas the Pt_xAu_{1-x} DENs were dialyzed. The presence of trace amounts of Cl^- (<0.1 mM) in the Cu UPD solution is known to stabilize the Cu adlayer leading to the observed positive shift of E_{UPD} for Pd_xAu_{1-x} DENs.[47]

Catalytic Hydrogenation Activity. The M_xAu_{1-x} (M = Pt or Pd) random alloy DENs described in the previous section were used to test the effectiveness of the strategy for predicting catalytic activity described in the Introduction and summarized by the white dashed line in Figure 1. Solution-phase hydrogenation of AA by H_2 was chosen as the model reaction for three reasons: (1) we have prior experience using it with DENs, (2) it is relatively simple, and (3) AA is soluble in water.[27,30,31,48] As discussed in the Experimental Section, the catalytic hydrogenation activity of the M_xAu_{1-x} DENs was determined by measuring the rate of H_2 consumption in a sealed reaction flask containing H_2 gas, AA, and M_xAu_{1-x} DENs. A photograph of the hydrogenation apparatus is provided in Figure S9.

Figure 3a shows how the H_2 pressure (ΔP_{H_2}) inside the reaction flask changes as a function of time for the Pt_xAu_{1-x} DENs. For all compositions, ΔP_{H_2} varies linearly with time during the 220 s period of the experiment, indicating constant reaction rates and no adverse deactivation or catalytically important structural changes of the DENs. TEM size analysis of Pt_xAu_{1-x} DENs (Figure S10) is consistent with our contention that there is no significant difference in DEN size before and after catalysis.

The slopes of the plots of ΔP_{H_2} vs t, which are a representation of the catalytic activity of Pt_xAu_{1-x} DENs, decrease from 0.0075 psi/s at x = 1.0 to nearly zero at x = 0.1. To provide a more quantitative measure of activity, the slopes of the lines in Figure 3a were converted to turnover frequencies (TOFs), as shown in Figure 3b. Interestingly, the plot of TOF vs DEN composition is a straight line, meaning that the area-specific activity is first-order with respect to the concentration of Pt in Pt_xAu_{1-x} DENs.[49] The data also suggest that interactions between Pt and Au atoms in Pt_xAu_{1-x} DENs exert a minor influence over the hydrogenation activities. In other words, the addition of Au simply dilutes the surface concentration of active Pt-only sites, leading to lower hydrogenation activities. This finding is in contrast to the expectation of the volcano-plot-based design strategy, discussed earlier and summarized in Figure 1, which predicts that the PtAu bimetallic surfaces bind H and AA at more optimal strengths than pure Pt or pure Au sites thereby imparting higher activities.

AA hydrogenations were also carried out using Pd_xAu_{1-x} DEN catalysts, and the results are shown in Figure 3c. With
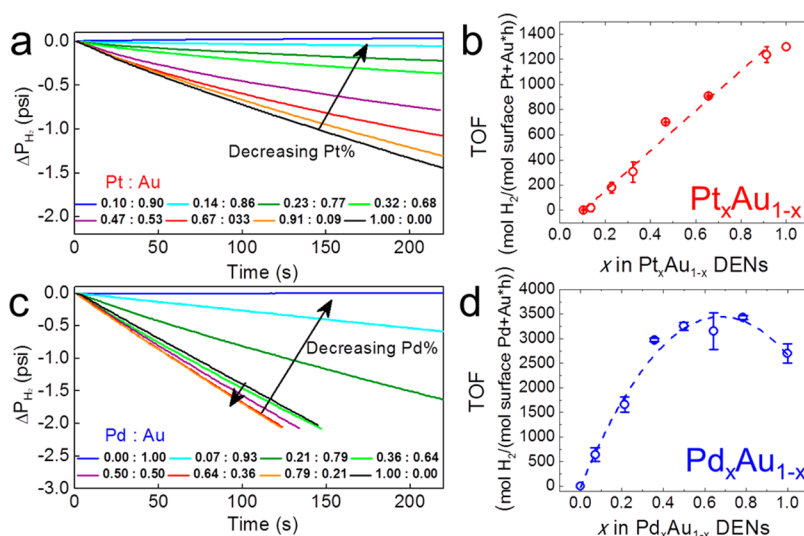
Figure 3. H$_2$ pressure change (ΔP_{H_2}) inside the sealed reaction flask as a function of reaction time for (a) Pt$_x$Au$_{1-x}$ and (c) Pd$_x$Au$_{1-x}$ DENs. The initial pressure and volume of H$_2$ were 1 atm and 116 mL, respectively. Reaction conditions: [AA] = 400 mM, [metal atoms] = 280 μM, AA−metal ratio = 10 000:7, T = 298 K, and the solvent was 25 mL of 80% v/v methanol. Turnover frequencies (TOFs) vs x for (b) Pt$_x$Au$_{1-x}$ and (d) Pd$_x$Au$_{1-x}$ DENs corresponding to the data shown in panels a and c, respectively. The error bars represent the standard deviations of duplicate measurements.

decreasing mole fraction of Pd, the slope initially increases (x = 1.0 to 0.64) and then rapidly decreases to 0 (x = 0). This behavior is in contrast to the monotonic decrease observed for the Pt$_x$Au$_{1-x}$ DENs. The plot of TOF vs x for the Pd$_x$Au$_{1-x}$ DENs exhibits a parabolic shape having a maximum TOF of 3500 mol H$_2$/(mol surface Pd+Au·h) at a Pd content of ~65%. This represents a ~30% activity improvement relative to the corresponding Pd-only DENs. This rate enhancement is in qualitative accord with the prediction of Figure 1 as well as previous reports by our groups and others for PdAu bimetallic catalysts having a range of different sizes.[26,27,50,51]

The higher TOF for the bimetallic PdAu nanoparticles than that for monometallic Pd and Au nanoparticles was previously attributed to charge transfer from Pd atoms to Au atoms, which was thought to increase the binding energy between Pd and olefins.[52] However, as we discussed in relation to Figure 1, pure Pd is not at the point of maximum activity because the AA binding energy to the Pd-only surface is too strong for optimal catalysis. Therefore, even higher binding energies between Pd and olefin, as suggested by the previously proposed mechanism,[52] are unlikely to cause improved hydrogenation activity.

DFT Calculations. Thus far, we have discussed the relationship between the structures of Pt$_x$Au$_{1-x}$ and Pd$_x$Au$_{1-x}$ DENs and their hydrogenation activity trends, and in this section we interpret these trends using first-principles theory. As previously discussed, the expected performance enhancement of alloy DENs is based on the hypothesis that the $E_{H,b}$ and $E_{AA,b}$ could be moved closer to the optimal values by mixing Au with Pt or Pd. The volcano-shaped TOF curve for the Pd$_x$Au$_{1-x}$ DENs (Figure 3d) confirms this expectation, but the linear TOF curve of Pt$_x$Au$_{1-x}$ DENs (Figure 3b) does not. This discrepancy between experimental findings and theoretical prediction motivates us to directly examine the adsorption of H and AA on the surfaces of these alloy DENs.

We begin this part of the study by examining the adsorption of H on an atomistic model of Pt$_x$Au$_{1-x}$ DENs using first-principles calculations. The model employed is a truncated octahedron containing 140 randomly distributed atoms (Figure

4a). We have previously shown that binding energies are only slightly affected by the alloy composition but that the local
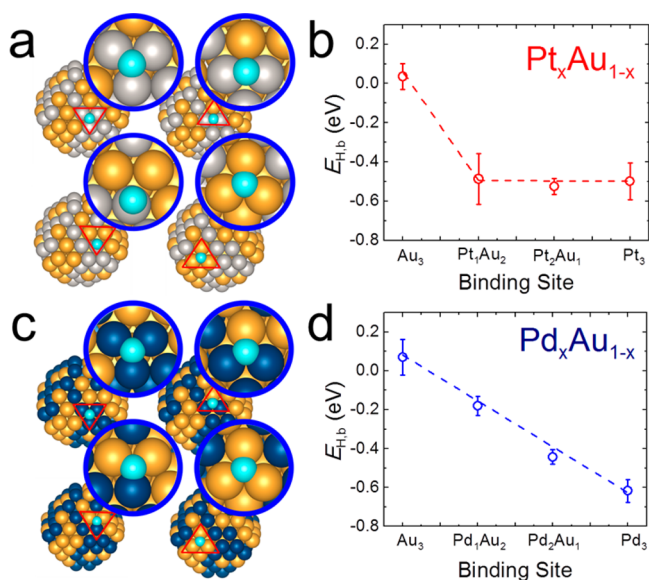

Figure 4. Representative optimal H binding geometry at four H-binding ensembles of (a) Pt$_x$Au$_{1-x}$ and (c) Pd$_x$Au$_{1-x}$ 140-atom models. The color key is as follows: Pt (gray), Au (gold), Pd (dark blue), and H (light blue). Calculated $E_{H,b}$ at different triatomic ensembles on (b) Pt$_x$Au$_{1-x}$ and (d) Pd$_x$Au$_{1-x}$ 140-atom models. The error bars represent the standard deviations of the H-binding energy for 10 randomly determined binding sites at different locations on the nanoparticle surface.

bonding environment (e.g., the surface ensemble) exerts a significant influence.[25,26] Therefore, we focus on just local structure and use a Pt:Au ratio of 1:1 to represent all possible compositions. In addition, we further simplified the calculations by considering that there are four major surface triatomic ensembles, which are Pt$_3$, Pt$_2$Au$_1$, Pt$_1$Au$_2$, and Au$_3$. Note that, due to the presence of under-coordinated sites on DENs (e.g.,

edges and vertices), $E_{H,b}$ at the same ensemble configuration might not be the same. Accordingly, 10 ensembles were randomly selected at different locations on the surface of the model nanoparticle, and then the average $E_{H,b}$ and its standard deviation were calculated.

The calculated $E_{H,b}$ for the PtAu ensembles are plotted in Figure 4b. The results show that $E_{H,b}$ remains roughly constant as long as a Pt atom is present in the ensemble. This indicates that the addition of Au to the Pt surface does not significantly affect $E_{H,b}$. This finding can be understood by considering the binding geometry of H_{ads} at the four ensembles. Specifically, Figure 4a shows that H_{ads} is not stable at the 3-fold hollow sites of Pt_2Au_1 and Pt_1Au_2 ensembles. Instead, H_{ads} relaxes to Pt−Pt bridge or Pt atop sites. In other words, H_{ads} does not directly interact with Au atoms in the Pt_2Au_1 and Pt_1Au_2 ensembles, and this means that Au substitution for Pt does not provide a means for tuning H_{ads}.

Similar calculations of H binding were carried out for PdAu ensembles (Figure 4c), and Figure 4d shows the average $E_{H,b}$ at each of the four relevant atomic ensembles. The linear dependence of $E_{H,b}$ on the number of Au atoms in the ensemble suggests that in this case Au does contribute to H binding. In fact, as shown in Figure 4c, H_{ads} remains at the 3-fold hollow sites for all ensembles rather than exhibiting a preference for the Pd sites.

In contrast to the striking difference between H binding on the different PtAu and PdAu ensembles, AA binding is quite similar for both alloys (Figure 5). In this case, the C−C double
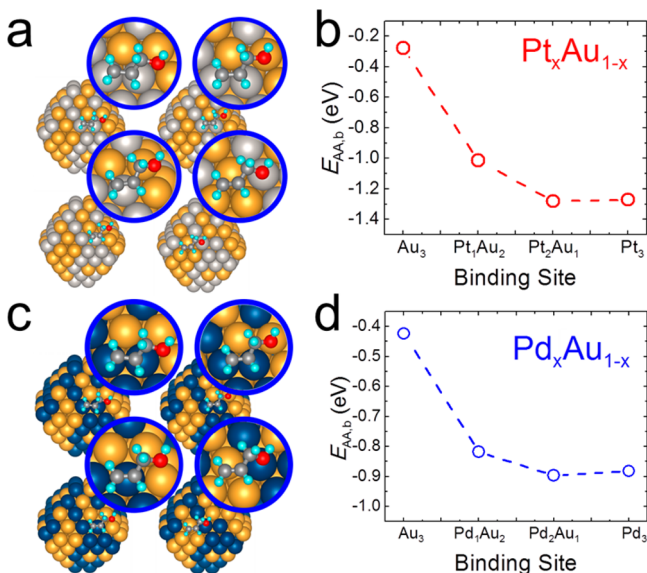
At the MAu_2 ensemble, however, AA is forced to adopt a π adsorption mode, in which C−C is adsorbed to a single Pt or Pd atom. This destabilizes AA binding by 0.1−0.2 eV relative to the di-σ adsorption mode. We conclude that $E_{AA,b}$ is not very sensitive to Au alloying with Pt or Pd, because the C−C bonds dock solely with Pt or Pd atoms through either di-σ or π configuration. It should be noted that we only examined AA adsorption at one typical binding site of the nanoparticle model for each surface ensemble due to high computational overhead.

On the basis of the calculations described above, we assessed the activities of all MAu ensembles using the previously discussed volcano plot. Figure 6 shows that Pt_3, Pt_2Au_1, and
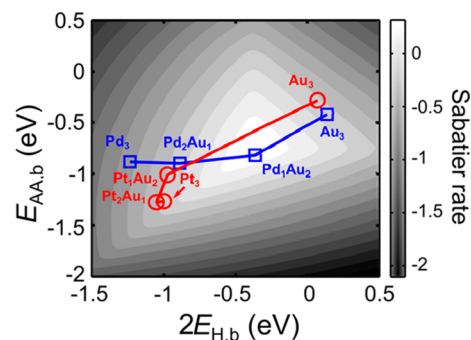

Figure 6. Contour plot of the Sabatier rate as a function of $E_{H,b}$ and $E_{AA,b}$ at Pt_xAu_{1-x} (red circles) and Pd_xAu_{1-x} ensembles (blue squares).

Pt_1Au_2 cluster together, meaning that PtAu ensembles exhibit no activity enhancement compared to Pt-only sites. This means that the hydrogenation activity of Pt_xAu_{1-x} alloy DENs is expected to monotonically decrease as the inactive Au content increases, while the number of active Pt sites decreases. This theoretical prediction is in a good agreement with the experimental observations. For Pd_xAu_{1-x} alloy DENs, however, the Pd_2Au_1 and Pd_1Au_2 ensembles are significantly more active than Pd_3 due to the lower $E_{H,b}$ resulting from the H−Au interactions. In particular, the Pd_1Au_2 ensemble is almost at the maximum activity predicted by the volcano plot. Thus, there should be an optimal DEN composition that maximizes the number of these more active sites on the Pd_xAu_{1-x} DENs, leading to the volcano-shaped activity vs composition plot observed in Figure 3d.

Tunability of H Binding. Up to this point we have interpreted the experimentally determined activity trends for Pt_xAu_{1-x} and Pd_xAu_{1-x} DENs in terms of the tunability of $E_{H,b}$ from a purely theoretical perspective. In this section, however, we will confirm the theoretical results using experiments that rely on measurements of the surface coverage (θ_H) of H_{ads}.

Figure 7a shows the theoretically predicted θ_H as a function of the fraction of M (M = Pt or Pd) on the MAu alloy surfaces, taking into account the H binding tunability effect discussed in the previous section. The computational details are provided in the SI. In the case of M = Pt, θ_H increases linearly as a function of the percentage of Pt on the DEN surface (red circles). A closer look at the distribution of H_{ads} on PtAu alloy surface reveals that it only resides at Pt_3 hollow sites and Pt−Pt bridge sites (Figure 7a top inset). These binding geometries are consistent with the finding shown in Figure 4 for H binding at different PtAu ensembles.

In contrast to PtAu, θ_H on the PdAu alloys decrease as a cubic function of the Au composition (blue circles in Figure 7a). Moreover, H_{ads} is located at both Pd_3 and Pd_2Au_1 3-fold

Figure 5. Calculated optimal AA binding geometry at four different ensembles of (a) Pt_xAu_{1-x} and (c) Pd_xAu_{1-x} 140-atom models, respectively. The color key is as follows: Pt (gray), Au (gold), Pd (dark blue), C (dark gray), O (red), and H (light blue). Corresponding $E_{AA,b}$ at different triatomic ensembles on (b) Pt_xAu_{1-x} and (d) Pd_xAu_{1-x}. No error bar is associated with the calculated $E_{AA,b}$ due to high computational overhead.

bond of AA prefers docking via the di-σ adsorption mode on M_3 and M_2Au ensembles (M = Pt or Pd). In this configuration, the two C atoms in the C−C bond are attached to two metal atoms on the surface, resulting in the formation of two C-M σ bonds. Moreover, $E_{AA,b}$ for the M_3 and M_2Au ensembles are nearly the same as a result of the similar adsorption geometry.
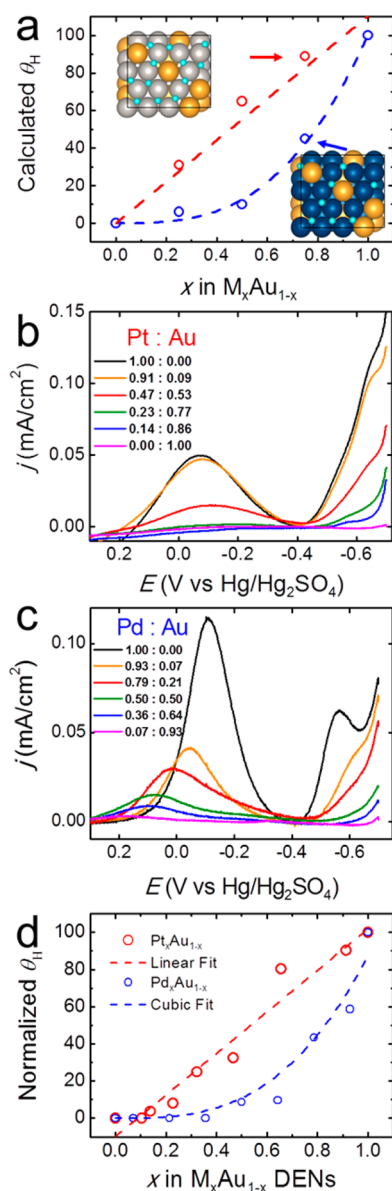
Figure 7. (a) Calculated surface coverage of H (θ_H) at a fixed chemical potential vs x in M_xAu_{1-x} DENs. Insets: calculated H coverage and distribution at $x = 0.75$ for a M_xAu_{1-x} slab surface. The color key is as follows: Pt (gray), Au (gold), Pd (dark blue), and H (light blue). Calculation methods and more details are provided in the SI. Voltammetric responses during the formation of H_{ads} and reduction of metal oxide at (b) Pt_xAu_{1-x} and (c) Pd_xAu_{1-x} DENs. The solution was deaerated 0.1 M $HClO_4$ solution, and the scan rate was 100 mV/s. The current is normalized to the electrochemically active surface area calculated from UPD Cu stripping voltammograms. (d) Normalized experimentally measured θ_H vs x in M_xAu_{1-x} DENs. H coverage was calculated from the total charge of H_{ads} and then normalized to the H coverage at Pt-only or Pd-only DENs. The red dashed line is the best linear fit of the data points, and the blue dashed line is the best cubic fit.

hollow sites (bottom inset), which is also consistent with results presented in the previous section. The reason for the more rapid decrease of θ_H on the PdAu alloys compared to the PtAu alloys is that PdAu bimetallic ensembles have a weaker $E_{H,b}$, than Pd_3. To summarize, PtAu and PdAu DENs are predicted to exhibit, respectively, linear and cubic relationships of θ_H and the percentage of Pt and Pd, respectively, on the DEN surface.

The values of θ_H on the M_xAu_{1-x} DEN surfaces were determined experimentally by measuring the amount of H by electrochemistry. Figure 7b shows voltammograms obtained for Pt_xAu_{1-x} DENs ($x = 0, 0.14, 0.23, 0.47, 0.91,$ and 1.00) in 0.10 M $HClO_4$ after subtraction of the capacitive background current. These scans were obtained by cycling the electrode potential three times between 0.60 V and −0.70 at 0.10 V/s, but data are only displayed for the final scan obtained at the end of the third cycle, which started at 0.30 V and ended at −0.70 V.

The voltammograms show that H adsorbs onto the Pt-only DENs between −0.40 V and −0.68 V, in the potential range just positive of the onset of bulk H_2 evolution, whereas no charge due to H adsorption is observed on Au-only DENs. This observation is consistent with previous reports.[32,53] The charge due to the adsorption of H atoms onto the Pt_xAu_{1-x} alloy DENs is the intermediate between that of Au-only and Pt-only DENs.[39] The red circles in Figure 7d show that the coverage of H varies linearly with fractional coverage of Pt on the Pt_xAu_{1-x} DEN surfaces.

The surface coverages of H_{ads} on the Pd_xAu_{1-x} DENs were also determined by integrating the voltammetric peak associated with H adsorption, situated between −0.40 V and −0.64 V in Figure 7c. The results are plotted as the blue circles in Figure 7d, and they show that the normalized values of θ_H are a cubic function of the Pd content of the Pd_xAu_{1-x} DENs. Note the good agreement between the theoretical calculations shown in Figure 7a and the experimentally determined values presented in Figure 7d. This correspondence confirms our hypothesis that the difference in the AA hydrogenation activity trends for the Pt_xAu_{1-x} and Pd_xAu_{1-x} DENs is primarily a function of the strength of the binding of H atoms. The most important finding, however, is that this binding energy can be tuned in some cases (e.g., Pd_xAu_{1-x}), but not in others (e.g., Pt_xAu_{1-x}).

■ SUMMARY AND CONCLUSIONS

In conclusion, we have shown that Pt_xAu_{1-x} and Pd_xAu_{1-x} DENs exhibit different activity trends for AA catalytic hydrogenation as a function of composition. Both experimental and theoretical results suggest that this behavior can be attributed to the binding energy of H atoms present on the catalytic Pt_xAu_{1-x} and Pd_xAu_{1-x} alloy surfaces. The interesting result is that the influence exerted on H_{ads} by the two different bimetallic surfaces is different. On the Pt_xAu_{1-x} DENs, H_{ads} is restricted to Pt-only surface sites, and therefore Au atoms simply act as a surface diluent. That is, H_{ads} only interacts with Pt, and hence its binding energy is unaffected by nearby Au atoms. In contrast, H_{ads} interacts with both Pd and Au atoms on the Pd_xAu_{1-x} DEN surface. Importantly, this provides a means for tuning the binding energy strength of H_{ads} and hence the hydrogenation activity of the PdAu bimetallic surface.

These findings are significant, because they provide new guidance for designing bimetallic alloy catalysts. Specifically, they suggest that the general approach to catalyst design strategy represented by the white dashed line in Figure 1 is not appropriate for some types of bimetallic surfaces. A complete understanding of bimetallic catalysts is more complex and requires a detailed knowledge of reactant interactions with specific atomic ensembles present on the surface. This can only be obtained by combining theory with well-defined experimental models like those reported here.

■ EXPERIMENTAL SECTION

Electronic Structure Calculations. Plane-wave-based density functional theory (DFT) calculations were performed using the Vienna ab initio simulation package.[54−56] The exchange correlation energy was described within the generalized gradient approximation using the Perdew−Burke−Ernzerhof functional.[57] The interaction between the valence electrons and the ionic electrons was treated within the projected augmented wave framework.[58] The Kohn−Sham orbitals were expanded in a plane-wave basis with a kinetic energy cutoff of 400 eV. The Brillouin zone was sampled by a $4 \times 4 \times 1$ grid of k points following the Monkhorst−Pack scheme.[59] A threshold of 10^{-5} eV was used for the convergence of the electronic structure. Optimized structures were obtained by minimizing the forces on each ion until they fell below 0.01 eV/Å. Transition states were determined with the climbing image nudged elastic band method.[60] In these calculations, the reaction paths were considered converged when all the forces on the images along the paths fell below 0.05 eV/Å.

The energy landscapes of the AA hydrogenation reaction were evaluated on different metal surfaces (Pd, Pt, Rh, Ir, Ru, Ni, Co, Cu, Ag, and Au) to construct the 2D-volcano plot (Figure 1), which correlates the catalytic activity with the binding energies of reactants. Metal surfaces were modeled with four-layer slabs separated by 12 Å of vacuum. The top two layers were allowed to relax, and the bottom two layers were kept fixed at the bulk positions. The supercell in the xy-plane had a geometry of $4 \times 2\sqrt{3}$ R90°, which contains 16 metal atoms in each layer of the slab model. Ru and Co were treated with hcp symmetry, whereas all other metals were treated with fcc symmetry. The corresponding (0001) and (111) surfaces were cut from the theoretical bulk lattices. The calculations with Ni and Co were spin-polarized, whereas all other metal were considered nonmagnetic where the reactants and products have closed electronic shells. To probe the effect of size reduction on the energetics of molecular binding strength, and thereby have a direct comparison between theory and experiment, we also employed a nanoparticle model for various metals and alloys to calculate the binding energies of reactants. The nanoparticle model had a truncated octahedral shape containing 140 atoms.

Chemicals. Sixth-generation, hydroxyl-terminated poly-(amidoamine) dendrimers (G6OH) in methanol were purchased from Dendritech, Inc. (Midland, MI). The methanol was removed under vacuum, and deionized (DI) water was added to yield a solution concentration of 200.0 μM. The following chemicals were used as received without further purification: $HAuCl_4 \cdot 3H_2O$, K_2PtCl_4, K_2PdCl_4, and $NaBH_4$ (Sigma-Aldrich), allyl alcohol (99+%, Aldrich), $CuSO_4$ (Fisher Scientific), and $HClO_4$ (70%, ULTREX II ultrapure reagent, J. T. Baker). Ultrahigh-purity (99.999%) H_2 gas was purchased from Praxair. Solutions were prepared using DI water from a Millipore Milli-Q water system (18.2 MΩ·cm).

DEN Synthesis. PdAu alloy, Pd, and Au DENs were prepared by adding n equivalents of K_2PdCl_4 (for PdAu alloy DENs, n = 10, 30, 50, 70, 90, 110, and 130; for Pd DENs, n = 140; and for Au DENs, n = 0) to a 10.0 μM aqueous solution of G6OH dendrimer. $PdCl_4^{2-}$ was allowed to complex with the dendrimers for 15.0 min, while N_2 was bubbled to exclude O_2 from the solution. $(140 - n)$ equivalents of $HAuCl_4$ were then added. Within 2 min, a 10-fold excess of $NaBH_4$ in 0.30 M NaOH was added to reduce the dendrimer−metal ion complexes to PdAu alloy DENs. The PdAu DEN solutions were kept under N_2 until used for hydrogenation reactions or structural characterization.

PtAu alloy DENs and Pt DENs were prepared following a procedure similar to that described in the previous paragraph, except for the following three exceptions. First, K_2PtCl_4 was complexed to the dendrimers for 3 days rather than 15 min.[34] Second, after adding $NaBH_4$, the reaction vessel was sealed, and the reaction was allowed to react for 2 days. Third, the PtAu DEN solutions were dialyzed for 24 h using cellulose dialysis sacks (MW cutoff of 12000, Sigma-Aldrich).

TEM Size Analysis. TEM images of all DENs were obtained using a JEOL 2010F TEM. The samples were prepared by dropping ~1 μL freshly prepared DEN ink (see next section) onto carbon-coated copper TEM grids (400 mesh, Electron Microscopy Sciences) and then drying with a N_2 stream (<1 min).

Electrochemistry. Electrochemical measurements were carried out using a CH Instruments model 1202B potentiostat (Austin, TX). A Hg/Hg_2SO_4 reference electrode, a Pt counter electrode, and a 3.0 mm diameter glassy carbon (GC) working electrode (all from CH Instruments) were used for all experiments.

DENs were immobilized onto the GC working electrode using a previously described procedure.[32] Briefly, the GC working electrode was prepared by successive polishing with 1.0, 0.3, and 0.05 μm alumina powder (Buehler) and then sonicated for 5 min to remove the polishing materials from the electrode surface. Next, Vulcan EC-72R carbon (1.0 mg per 1.0 mL) was added to the DEN solution, and the mixture was sonicated for 5 min to yield a DEN ink. Finally, a 5.0 μL aliquot of the DEN ink was pipetted onto the clean GC and then dried under flowing N_2. Next, the electrode was immediately immersed in 10.0 mL of deaerated 0.10 M $HClO_4$.

The following electrochemical measurements were successively carried out using the same DEN-modified working electrode. First, the surface of the DENs was cleaned by cycling the DEN-modified GC working electrode potential between 0.50 V and −0.70 V vs Hg/Hg_2SO_4 in 0.10 M N_2-purged $HClO_4$ at a scan rate of 200 mV/s until the voltammograms no longer changed (>10 scans). Second, cyclic voltammograms (CVs) of the DEN-modified GC electrode were recorded in the same $HClO_4$ at a scan rate of 100 mV/s. The potential was swept between 0.60 and −0.70 V for PtAu alloy DENs and between 0.50 and −0.70 V for PdAu alloy DENs. The starting potential for these scans was 0 V; the initial scan direction was positive, and the final potential was −0.70 V. Third, 100 μL of 0.50 M $CuSO_4$ was added to the $HClO_4$ solution. This step was carried out with the working electrode immersed in the $HClO_4$ cleaning solution and at the open-circuit potential (OCP). The electrode potential was then stepped from the OCP to the Cu UPD potential (−0.38 V vs Hg/Hg_2SO_4 for PtAu alloy DENs and −0.40 V for PdAu alloy DENs) and held for 100 s. Finally, the potential of DEN-modified GC working electrode was swept from the UPD potential to 0.15 V at 10.0 mV/s. The resulting UPD Cu stripping voltammograms were recorded.

Hydrogenation Reactions. Hydrogenation experiments were carried out using a home-built hydrogenation apparatus. A photograph of the system is provided in Figure S9. The reaction was carried out in a 100 mL three-neck round-bottom flask. One neck of the flask was connected to a tank of H_2; the second was sealed by a rubber septum and used for regent addition, and the third was attached to a glass bubbler and Extech HD700 differential pressure manometer through a glass three-way stopcock. The Extech manometer was connected to a PC with a USB cable for real-time data recording.

Prior to hydrogenation reactions, the pH of the freshly prepared DEN solution was lowered to 5.5 with 0.10 M $HClO_4$ to deactivate unreacted $NaBH_4$.[61] Next, 5.0 mL of the pH-adjusted DEN solution plus 20 mL of methanol and a magnetic stir bar were added to the round-bottom flask. The joints of the apparatus were sealed with silicone grease and checked for leaks before adding the substrate (AA). The system was purged with H_2 for 10 min while stirring the solution. The system was then sealed by closing the stopcocks, and then the solution was stirred for an additional 10 min or until the H_2 pressure inside the flask reached a constant value. Experiments were initiated by adding 10 mmol (680 μL) of AA by syringe with vigorous stirring (1500 rpm). Stirring was maintained at this rate throughout the hydrogenation reactions. The H_2 pressure was recorded every second using software provided by Extech.

■ ASSOCIATED CONTENT

Ⓢ Supporting Information

The Supporting Information is available free of charge on the ACS Publications website at DOI: 10.1021/jacs.7b01653.

> Method for generating volcano plots for AA hydrogenation; a discussion of incomplete reduction of $PtCl_4^{2-}$ within dendrimers; TEM and STEM images of DENs;

UPD Cu stripping voltammograms for physical mixtures of Pt-only and Au only DENs, and for Au@Pt DENs; photograph and description of the hydrogenation system; TEM micrographs and size distribution histograms of DENs before and after hydrogenation reactions; determination of H_{ads} coverage; and electrochemical adsorption and absorption of H for Pd DENs (PDF)

■ AUTHOR INFORMATION

Corresponding Authors
*henkelman@utexas.edu
*crooks@cm.utexas.edu
ORCID
Graeme Henkelman: 0000-0002-0336-7153
Richard M. Crooks: 0000-0001-5186-4878

Author Contributions
[⊥]L.L. and Z.D. contributed equally.

Notes
The authors declare no competing financial interest.

■ ACKNOWLEDGMENTS

■ REFERENCES

(1) Herrmann, U.; Emig, G. *Ind. Eng. Chem. Res.* **1997**, *36*, 2885.
(2) Yuan, X.; Zheng, J.; Zhang, Q.; Li, S.; Yang, Y.; Gong, J. *AIChE J.* **2014**, *60*, 3300.
(3) Campo, B. C.; Volpe, M. A.; Gigola, C. E. *Ind. Eng. Chem. Res.* **2009**, *48*, 10234.
(4) Freeman, I. P. In *Ullmann's Encyclopedia of Industrial Chemistry*; Wiley-VCH Verlag GmbH & Co. KGaA, 2000.
(5) Rylander, P. N. In *Ullmann's Encyclopedia of Industrial Chemistry*; Wiley-VCH Verlag GmbH & Co. KGaA, 2000.
(6) Best, R. J.; Russell, W. W. *J. Am. Chem. Soc.* **1954**, *76*, 838.
(7) Yoshida, S.; Yamashita, H.; Funabiki, T.; Yonezawa, T. *J. Chem. Soc., Faraday Trans. 1* **1984**, *80*, 1435.
(8) Ponec, V. In *Advances in Catalysis*; Eley, D. D., Pines, H., Weisz, P., Eds.; Academic Press, 1983; Vol. 32, p 149.
(9) Schwank, J. *Gold Bull.* **1985**, *18*, 2.
(10) Ponec, V. *Appl. Catal., A* **2001**, *222*, 31.
(11) Sinfelt, J. H. *Acc. Chem. Res.* **1977**, *10*, 15.
(12) Chen, T.; Rodionov, V. O. *ACS Catal.* **2016**, *6*, 4025.
(13) Zhang, J.; Chen, G.; Guay, D.; Chaker, M.; Ma, D. *Nanoscale* **2014**, *6*, 2125.
(14) Studt, F.; Abild-Pedersen, F.; Bligaard, T.; Sørensen, R. Z.; Christensen, C. H.; Nørskov, J. K. *Science* **2008**, *320*, 1320.
(15) Chen, M.; Kumar, D.; Yi, C.-W.; Goodman, D. W. *Science* **2005**, *310*, 291.
(16) Clarke, J. K. A. *Chem. Rev. (Washington, DC, U. S.)* **1975**, *75*, 291.
(17) Hall, W. K.; Emmett, P. H. *J. Phys. Chem.* **1959**, *63*, 1102.
(18) Gharpurey, M. K.; Emmett, P. H. *J. Phys. Chem.* **1961**, *65*, 1182.
(19) Dowden, D. A. *J. Chem. Soc.* **1950**, 242.
(20) Mavrikakis, M.; Hammer, B.; Nørskov, J. K. *Phys. Rev. Lett.* **1998**, *81*, 2819.
(21) Heard, C. J.; Hu, C.; Skoglundh, M.; Creaser, D.; Grönbeck, H. *ACS Catal.* **2016**, *6*, 3277.
(22) Heard, C. J.; Siahrostami, S.; Grönbeck, H. *J. Phys. Chem. C* **2016**, *120*, 995.
(23) Neurock, M.; van Santen, R. A. *J. Phys. Chem. B* **2000**, *104*, 11127.
(24) Miura, T.; Kobayashi, H.; Domen, K. *J. Phys. Chem. B* **2000**, *104*, 6809.
(25) García, S.; Zhang, L.; Piburn, G. W.; Henkelman, G.; Humphrey, S. M. *ACS Nano* **2014**, *8*, 11512.
(26) Kunal, P.; Li, H.; Dewing, B. L.; Zhang, L.; Jarvis, K.; Henkelman, G.; Humphrey, S. M. *ACS Catal.* **2016**, *6*, 4882.
(27) Scott, R. W. J.; Wilson, O. M.; Oh, S.-K.; Kenik, E. A.; Crooks, R. M. *J. Am. Chem. Soc.* **2004**, *126*, 15583.
(28) Myers, V. S.; Weir, M. G.; Carino, E. V.; Yancey, D. F.; Pande, S.; Crooks, R. M. *Chem. Sci.* **2011**, *2*, 1632.
(29) Niu, Y.; Crooks, R. M. *C. R. Chim.* **2003**, *6*, 1049.
(30) Wilson, O. M.; Knecht, M. R.; Garcia-Martinez, J. C.; Crooks, R. M. *J. Am. Chem. Soc.* **2006**, *128*, 4510.
(31) Niu, Y.; Yeung, L. K.; Crooks, R. M. *J. Am. Chem. Soc.* **2001**, *123*, 6840.
(32) Luo, L.; Zhang, L.; Henkelman, G.; Crooks, R. M. *J. Phys. Chem. Lett.* **2015**, *6*, 2562.
(33) Knecht, M. R.; Weir, M. G.; Frenkel, A. I.; Crooks, R. M. *Chem. Mater.* **2008**, *20*, 1019.
(34) Knecht, M. R.; Weir, M. G.; Myers, V. S.; Pyrz, W. D.; Ye, H.; Petkov, V.; Buttrey, D. J.; Frenkel, A. I.; Crooks, R. M. *Chem. Mater.* **2008**, *20*, 5218.
(35) Zhang, L.; Iyyamperumal, R.; Yancey, D. F.; Crooks, R. M.; Henkelman, G. *ACS Nano* **2013**, *7*, 9168.
(36) Petkov, V.; Wanjala, B. N.; Loukrakpam, R.; Luo, J.; Yang, L.; Zhong, C.-J.; Shastri, S. *Nano Lett.* **2012**, *12*, 4289.
(37) Foiles, S. M.; Baskes, M. I.; Daw, M. S. *Phys. Rev. B: Condens. Matter Mater. Phys.* **1986**, *33*, 7983.
(38) Zhang, H.; Jin, M.; Xia, Y. *Chem. Soc. Rev.* **2012**, *41*, 8035.
(39) Suntivich, J.; Xu, Z.; Carlton, C. E.; Kim, J.; Han, B.; Lee, S. W.; Bonnet, N.; Marzari, N.; Allard, L. F.; Gasteiger, H. A.; Hamad-Schifferli, K.; Shao-Horn, Y. *J. Am. Chem. Soc.* **2013**, *135*, 7985.
(40) Anderson, R. M.; Zhang, L.; Loussaert, J. A.; Frenkel, A. I.; Henkelman, G.; Crooks, R. M. *ACS Nano* **2013**, *7*, 9345.
(41) Carino, E. V.; Crooks, R. M. *Langmuir* **2011**, *27*, 4227.
(42) Carino, E. V.; Kim, H. Y.; Henkelman, G.; Crooks, R. M. *J. Am. Chem. Soc.* **2012**, *134*, 4153.
(43) Menard, L. D.; Wang, Q.; Kang, J. H.; Sealey, A. J.; Girolami, G. S.; Teng, X.; Frenkel, A. I.; Nuzzo, R. G. *Phys. Rev. B: Condens. Matter Mater. Phys.* **2009**, *80*, 064111.
(44) Xing, Y.; Cai, Y.; Vukmirovic, M. B.; Zhou, W.-P.; Karan, H.; Wang, J. X.; Adzic, R. R. *J. Phys. Chem. Lett.* **2010**, *1*, 3238.
(45) Green, C. L.; Kucernak, A. *J. Phys. Chem. B* **2002**, *106*, 11446.
(46) Lu, Y.-C.; Xu, Z.; Gasteiger, H. A.; Chen, S.; Hamad-Schifferli, K.; Shao-Horn, Y. *J. Am. Chem. Soc.* **2010**, *132*, 12170.
(47) Möller, F. A.; Magnussen, O. M.; Behm, R. J. *Phys. Rev. B: Condens. Matter Mater. Phys.* **1995**, *51*, 2484.
(48) Scott, R. W. J.; Datye, A. K.; Crooks, R. M. *J. Am. Chem. Soc.* **2003**, *125*, 3708.
(49) McNaught, A. D.; McNaught, A. D. *Compendium of chemical terminology*; Blackwell Science: Oxford, 1997; Vol. *1669*.
(50) Toshima, N.; Harada, M.; Yamazaki, Y.; Asakura, K. *J. Phys. Chem.* **1992**, *96*, 9927.
(51) Mizukoshi, Y.; Fujimoto, T.; Nagata, Y.; Oshima, R.; Maeda, Y. *J. Phys. Chem. B* **2000**, *104*, 6028.
(52) Toshima, N.; Yonezawa, T. *New J. Chem.* **1998**, *22*, 1179.
(53) Ye, H.; Crooks, J. A.; Crooks, R. M. *Langmuir* **2007**, *23*, 11901.
(54) Kresse, G.; Hafner, J. *Phys. Rev. B: Condens. Matter Mater. Phys.* **1993**, *47*, 558.
(55) Kresse, G.; Furthmüller, J. *Comput. Mater. Sci.* **1996**, *6*, 15.
(56) Kresse, G.; Furthmüller, J. *Phys. Rev. B: Condens. Matter Mater. Phys.* **1996**, *54*, 11169.

(57) Perdew, J. P.; Burke, K.; Ernzerhof, M. *Phys. Rev. Lett.* **1996**, *77*, 3865.

(58) Blöchl, P. E. *Phys. Rev. B: Condens. Matter Mater. Phys.* **1994**, *50*, 17953.

(59) Monkhorst, H. J.; Pack, J. D. *Phys. Rev. B* **1976**, *13*, 5188.

(60) Henkelman, G.; Uberuaga, B. P.; Jónsson, H. *J. Chem. Phys.* **2000**, *113*, 9901.

(61) Anderson, R. M.; Yancey, D. F.; Loussaert, J. A.; Crooks, R. M. *Langmuir* **2014**, *30*, 15009.